Materials Characterization 160 (2020) 110075

Contents lists available at ScienceDirect

Materials Characterization

journal homepage: www.elsevier.com/locate/matchar

Characterization of nano-sized particles in 14%Cr oxide dispersion strengthened (ODS) steel using classical and frontier microscopy methods

Yael Templeman[a], Sergey Rogozhkin[b,c], Artem Khomich[b], Aleksander Nikitin[b,c], Malki Pinkas[d], Louisa Meshi[a,*]

[a] Department of Materials Engineering, Ben Gurion University of the Negev, POB 653, Beer Sheva 84105, Israel
[b] Institute for Theoretical and Experimental Physics named by A.I. Alikhanov of National Research Centre «Kurchatov Institute», 117218 Moscow, Russia
[c] National Research Nuclear University «MEPhI», 115409 Moscow, Russia
[d] Nuclear Research Center-Negev, P.O. Box 9001, Beer-Sheva, Israel

ARTICLE INFO

Keywords:
ODS steels
Transmission electron microscopy
Atom probe tomography
Oxide
Characterization

ABSTRACT

Oxide dispersion strengthened (ODS) steels exhibit superior mechanical properties and irradiation resistance due to nano-sized oxides, highly dispersed in the metallic matrix. The mechanical properties are affected by the structure, composition, size and density of the nano-sized oxides. Despite numerous reports on the characterization of these oxides, ambiguity regarding their composition, crystallographic structure and orientation relationship with the matrix remains. In the present study, characterization of the crystallographic structure of oxide particles existing in 14%Cr ODS steel was performed using classical and novel transmission electron microscopy (TEM) methods. 3D dispersion, density and composition of these oxides were evaluated by atom probe tomography (APT). Three populations of particles were detected: highly dispersed, 3–20 nm Fe(Cr,Ti,Y)O particles with spinel structure; 50–150 nm $YTiO_3$ and large (100–200 nm) particles identified as cubic TiC.

The spinel-type particles displayed Bain and Kurdjumov-Sachs orientation relationships (OR) with the ferritic matrix. Applying electron diffraction tomography, the $YTiO_3$ structure was attributed to the $GdFeO_3$ (distorted perovskite)-type and its lattice parameters were refined as a = 5.46 Å, b = 7.66 Å and c = 5.28 Å. Orientation relationship of the $YTiO_3$ particles and Fe matrix were determined as $[110]_{Fe}//[210]_{oxide}$ and $(110)_{Fe}//(002)_{oxide}$.

1. Introduction

For the next generation nuclear power plants, high performance structural alloys with exceptional properties at extreme conditions are required. Oxide dispersion strengthened (ODS) steels are promising candidates for such applications [1,2]. As it states from their name, these steels are reinforced by nano-sized oxide particles which improve dramatically the mechanical properties of the matrix. The oxides limit matrix's grain growth and block dislocation mobility which results in increased strength [3]. In addition, under neutron irradiation, the interfaces between the oxides and the Fe matrix serve as sinks for point defects such as vacancies and He bubbles, thus improving the radiation resistance of the steel [4,5].

ODS steels are prepared using mechanical alloying of Y_2O_3 with a powder consisting of Fe, Cr and additional alloying elements. The choice of Y_2O_3 is due to its high thermal stability [6]. The mechanical alloying causes Y_2O_3 to decompose into Y and O atoms, which in the following hot consolidation stage crystallize into complex oxides containing Y, O and transition metals [7,8]. For example, addition of Ti to ODS steels leads to the formation of Y—Ti oxides, which display an impressive stability under irradiation [2,9–11]. Ti also plays an important role in reducing the particles' size, leading to a higher dispersion of fine Y—Ti oxides [7].

Since the nano-oxides are responsible for the unique properties of the ODS steels, they have been studied extensively. The most common types of oxides reported for the Cr-rich ferritic ODS steels (containing Ti and Y) are the $Y_2Ti_2O_7$ and Y_2TiO_5 [5,7,12–15]. There is a dispute among different researchers regarding the type of orientation relationship (OR) of these oxides with the Fe-rich matrix. Exact composition of the Y_2TiO_5 and $Y_2Ti_2O_7$ is also a matter of discussion. Some researchers reported non-stoichiometric Y-Ti-O enriched clusters with varying Y/Ti ratio [12,16]. It should be noted that in addition to the $Y_2Ti_2O_7$ and Y_2TiO_5 phases, in the Y-Ti-O system - $YTiO_3$ oxide exists, but it was rarely documented in the literature with regard to ODS steels

* Corresponding author.
E-mail address: louisa@bgu.ac.il (L. Meshi).

https://doi.org/10.1016/j.matchar.2019.110075
Received 10 October 2019; Received in revised form 24 November 2019; Accepted 13 December 2019
Available online 17 December 2019

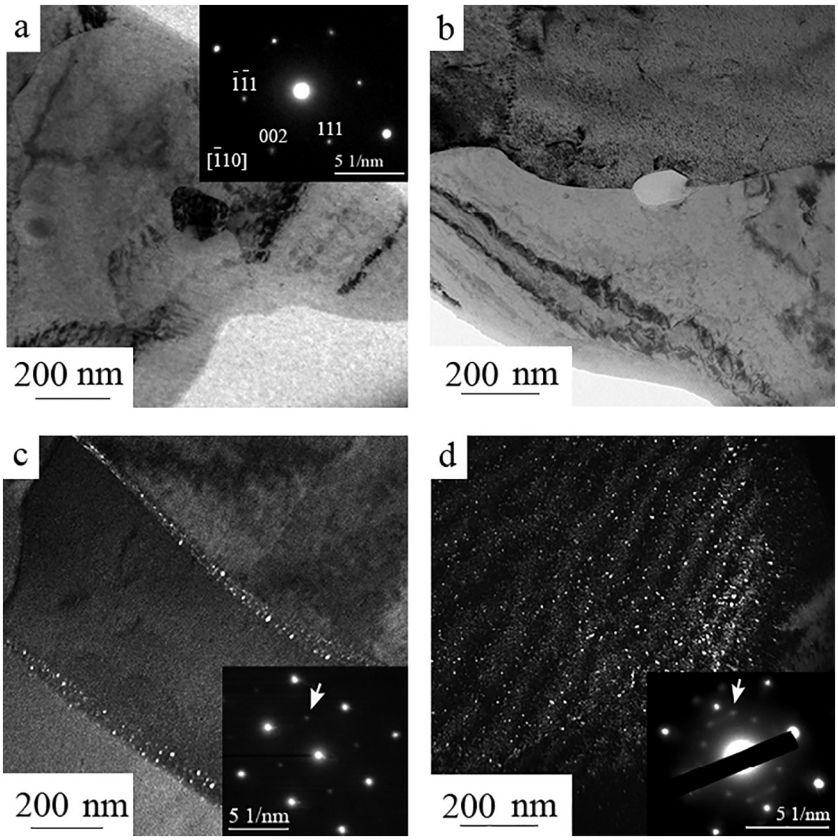

Fig. 1. Three populations of particles observed in the ODS steel: a) TiC particle with a size of 150 nm. ED pattern taken from this particle, indexed in terms of TiC FCC unit cell with a = 4.33 Å [27], is shown in the inset. b) Large 150 nm Y-Ti-O particle, located along a grain boundary. c) and d) DF images illustrating the nano-oxides along grain boundaries and at the grains' interior, respectively. Corresponding electron diffraction patterns are presented in the insets and the *g* vectors, used for DF images, are marked by arrows. The intense spots are indexed as Fe [001] zone axis pattern, less intense ones originate from the particles (for indexing of these patterns please refer to Fig. 8).

[17,18]. Furthermore, the strengthening oxides in ODS steels do not always adopt structures reported in the Y-Ti-O system. For example, Hirata *et al.* [19] found oxide particles composed of Ti(Y,Fe,Cr)-O, having a defective NaCl structure type, and exhibiting OR with the matrix. Sakasegawa reported the presence of Al_2O_3, Fe_3O_4 (Magnetite) and TiO_2 (Anatase) [12]. Thus, the numerous studies conducted on the oxide particles point to an ambiguity regarding their composition and structure. Further characterization using a combination of advanced methods may shed some light into this ambiguity.

Due to the nanometric size of the oxides, characterization of their crystallographic structure is challenging. Atom probe tomography (APT) is a powerful tool widely used to investigate the composition of the oxides at atomic scale, however it does not provide structural information and for this - additional methods are required. Indexing of conventional electron diffraction (ED) patterns obtained by transmission electron microscopy (TEM) is often challenging due to the large contribution of the matrix, and fast Fourier transform (FFT), taken from the high resolution TEM (HRTEM) images, are often ambiguously interpreted. In the present study, a detailed TEM investigation, applying classical and novel electron crystallography approaches, combined with APT analysis was performed in order to characterize the nano-oxide particles embedded in the ferritic matrix.

2. Experimental

The current study focuses on the characterization of the dispersed particals in a 14% Cr ferritic ODS steel provided by CEA/DEN/DANS. The nominal composition, as reported and verified by the Energy Dispersive Spectroscopy (EDS) in Scanning Electron Microscope (SEM), is Fe - 14wt%Cr - 1wt%W - 0.3wt%Ti - 0.25wt%Y_2O_3. The fabrication process included mechanical alloying (MA) of the powders, hot extrusion at 1100 °C, hot isostatic pressing (HIP) for 4 h at 1050 °C and 1400 bar and a final heat treatment at 1050 °C for 1 h. The mechanical properties of the investigated 14% Cr ODS steel are reported in [20,21].

TEM investigation was carried out using a 200 kV JEOL JEM 2011 FasTEM and a JEOL JEM-2100F TEM operating at 200 kV equipped with JED-2300 T EDS, scanning coils and GATAN 806 high angle annular dark field (HAADF) detector. Bulk specimens were sliced using an electric discharge machine (EDM) and polished down to 50 μm on a series of SiC lapping disks. The samples were cut into three millimeter discs in diameter and thinned to an electron transparency using Gatan Precision Ion Polishing System (PIPS). Electron diffraction tomography (EDT) datasets were collected manually by tilting the sample around an arbitrary axis and recording an ED pattern at 1° steps in the selected area electron diffraction (SAED) mode. In order to gain a wide angular range, a high tilt tomography holder (FISCHIONE) was used enabling a tilt angle of approximately ± 60°. Following the data collection, the series of ED frames were merged and processes using the EDT- process software [22].

For EDT analysis, extraction replica samples were prepared. The steel was immersed in a solution containing 50% HCl and 50% water in order to dissolve the Fe matrix, leaving only the oxide particles. Then, the solution was dropped on an Au TEM grid.

APT investigation was carried out with a laser-assisted tomographic atom probe (APPLE-3D) designed at the Institute of Theoretical and Experimental Physics (Moscow) [23]. Evaporation was induced by 515 nm laser with an energy of 0.1–1.2 μJ, pulsing at a 25 kHz frequency of 300 fs long pulses. The pressure was $(5 \div 7) \times 10^{-10}$ Torr and the specimen tip was kept at 40–50 K.

The reconstruction and analysis of the APT data included mass spectrum identification and characterization of 3D distribution of the chemical elements in the studied volumes. To describe the nano-scale features that were detected, the maximum separation algorithm was applied [24]. In this algorithm, the local environment of each atom, within a small sphere of a diameter d_{max}, was tested. If the number of atoms of a given solute element "A" in the sphere exceeded a threshold value of N_{min}, the sphere was regarded as an "A" cluster which center is at the center of the sphere. If another atom (marked B) was present in

the sphere belonging to this cluster, then the algorithm associated the two atoms to the same "A" cluster. This procedure performed on each individual atom of the analyzed volume, allowing the identification all the possible clusters. Finally a smoothing step was applied by attributing atoms of clusters that consist of less than N_0 atoms to the matrix [25,26]. If the selected values of D_{max} and N_{min} are too small, fragmentation of clusters is observed. A choice of too large values for D_{max} and N_{min} leads to the artificial joining of closely located clusters. In the current research, D_{max} and N_{min} were set at 0.8 nm and 7 atoms, respectively.

3. Results

The particles observed in the studied ODS steel could be classified into three main populations, easily distinguished by their characteristic dimensions. The largest particles and less frequently observed were identified as TiC with a typical size of 100–200 nm. An example of such particle is shown in Fig. 1a. EDS analysis and ED pattern (shown in the inset of Fig. 1a), taken from this particle, confirmed it to be a face centered cubic (FCC) TiC particle. The second type of particles, which were more frequently dispersed as compared to the TiC particles, were oxides with sizes in the range of 50–150 nm (Fig. 1b). According to the EDS analysis, these oxides are composed mainly of Y, Ti and O. The third population consists of densely distributed nano-sized particles, varying from several to 20 nm. Due to their nanometric size, they were difficult to detect on bright field (BF) TEM images. However, these particles were clearly observed in dark field (DF) images obtained from extra reflections (e.g. in addition to the Fe matrix) in the ED pattern. As can be seen in Fig. 1d and c, in some cases these nano-particles were preferably located at grain boundaries and in other cases at the grains' interior.

Due to the nanometric size of the small particles, the contribution of the surrounding matrix is too significant for a TEM EDS analysis. Atom Probe Tomography (APT) allowed obtaining atom maps from the investigated clusters, see Fig. 2a. The clusters' size was measured according to these maps as several nanometers, consistent with the TEM observations shown in Fig. 1c and d. The density of these clusters was quite high, measured as $\sim 10^{24}$ m^{-3}. Fig. 2b shows chemical composition of the investigated clusters. The nano-sized particles contain mainly O, Ti, Cr, a small amount of Y and Fe (balance). The ratios Y/Ti and (Y + Ti)/O were calculated to be ~0.3 and 1.5, respectively. For illustration, radial distribution of solutes in one of the clusters is presented in Fig. 3. Table 1 summarizes the chemical composition of the matrix compared to the clusters. It can be seen that concentrations of Cr, O, Ti, and Y are higher in the clusters relatively to the matrix. Although artifacts of the APT measurements [28] have possibly affected the quantification of the measurements and prevented precise determination of the composition, the fact that these cluster exist and that they contain Cr in addition to expected Ti, Y, and O is clear. Similarity between the TEM and APT observations provide additional support to this understanding.

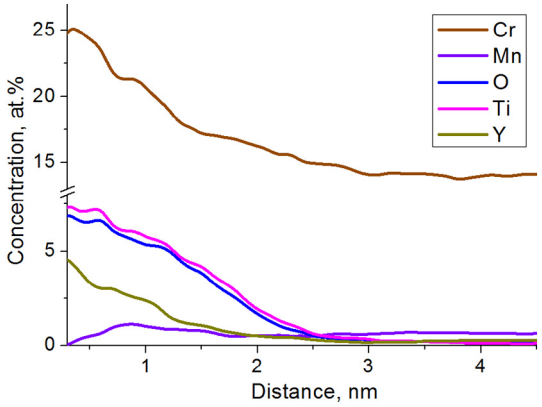

Fig. 3. Radial distribution of solutes in the 5-th cluster (as indexed in Fig. 2b). Composition was determined in a spherical layer of 1 Å thick (smoothing procedure was applied).

Table 1
Chemical composition (in at.%) of the matrix and the clusters, as measured by APT.

Element	Matrix		Clusters	
	at.%	± Δ	at.%	± Δ
C	0.04	0.01	0.08	0.07
O	0.08	0.02	5.8	0.8
Cr	15.2	0.3	22	2
Fe	83.2	0.3	62	2
W	0.19	0.03	0.3	0.2
Si	0.63	0.05	1.0	0.3
Ti	0.09	0.02	7	1
Mn	0.46	0.05	0.4	0.2
Y	–	–	1.6	0.4

To identify the structure of the 50–150 nm and 2-20 nm particles, which will further be referred to as "large" and "nano" sized oxides, respectively, electron crystallography methods were employed.

3.1. Structural characterization of larger particles

Characterization of the relatively large oxide particles was performed using Electron Diffraction Tomography (EDT) method [22,29–31], since indexing of conventional ED patterns, taken in the selected area (SAED) mode, was ambiguous. For the EDT analysis, extraction replica sample was prepared to eliminate the contribution of the matrix to the ED patterns and EDS measurements. Following manual data collection, the frames were merged, using the EDT-process

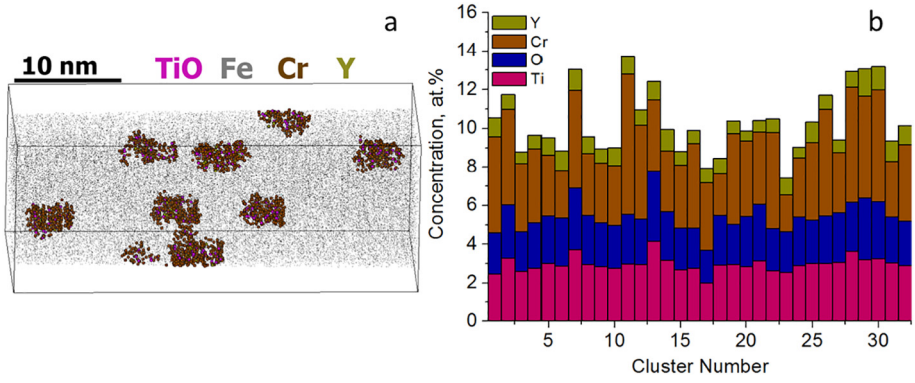

Fig. 2. a) Atom maps of investigated volume. b) Chemical composition of detected clusters with respect to the matrix.

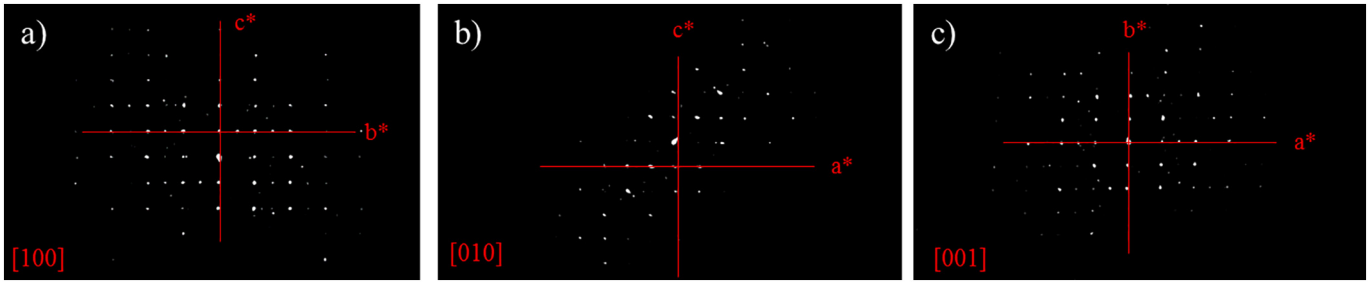

Fig. 4. Selected projections of the reconstructed reciprocal space (which exhibit the highest symmetry) were indexed as a) [100], b) [010] and c) [001].

Table 2
Unit cell parameters of the studied Y-Ti-O structure, extracted from the EDT data, and lattice parameters of the reported in [33] $YTiO_3$ structure.

	a [Å]	b [Å]	c [Å]	α	β	γ
EDT data	5.46	7.66	5.28	90.95°	90°	90°
$YTiO_3$ structure [33]	5.618	7.591	5.327	90°	90°	90°

software [22], which enables to reconstruct a 3D reciprocal space. Using a procedure described in [22], the reciprocal space can be rotated so that the highest symmetry projections will be detected. In this way, the geometry of the unit cell can be evaluated. It had been demonstrated that the routine of unit cell search is quite stable against a tilt-axis error [32], thus the error in the tilt axis causes very small deviations from the true lattice parameters. In our study tilt axis was determined by the cylindrical projection that is used for the determination of the goniometer tilt axis of the microscope. Following a successful reconstruction, a list of d_{hkl} and intensities was extracted. The projections of the highest symmetry, i.e. [100], [010] and [001] are shown in Fig. 4a-c, respectively. The extracted lattice parameters are presented in Table 2. The accuracy of the cell parameters` determination depends on the calibration and other systematic errors, the unit cell angles can be calculated with an accuracy of about 1° [31,32].

As can be seen from Table 2, $a \neq b \neq c$ and $\alpha \approx \beta \approx \gamma \approx 90°$. Thus, the crystal system was classified as orthorhombic. Analysis of the dataset intensities allowed deducing the following reflection conditions: *h00 h = 2n; 0 k0 k = 2n; 00 l l = 2n; hk0 h + k = 2n; 0kl k + l = 2n*. These conditions belong to the P*n_n* extinction (diffraction) symbol and indicate that the symmetry of this structure can be described either by the P*n*2*n* (34) or P*nmn* (58) space groups. According to the PDF4+ (2018) database (International Center for Diffraction Data) [33], the calculated lattice parameters are close to those of $YTiO_3$ with a distorted perovskite structure, which exhibit a P*nmn* space group, see Table 2. Therefore, the large oxides were attributed to this structure.

In order to prove that the particles in the matrix have the same structure as those in the replica, ED patterns taken from the particles embedded in the matrix (e.g. original bulk TEM sample) were analyzed. All patterns were successfully indexed in terms of the $YTiO_3$ structure using determined here lattice parameters. Some examples are shown in Fig. 5a-c. It should be noted that these patterns could not been indexed in terms of any other Y-Ti-O or Ti−O known structures. Moreover, as can be seen from Table 2, the lattice parameters determined by EDT were somewhat different from the JCPDF card of the $YTiO_3$ structure (number 04-001-7833).

3.2. Structure characterization of the nano-sized oxide particles

Crystallographic structure of the nano-sized oxides was determined using the superimposed matrix/oxide ED patterns. ED patterns taken from the matrix contained diffused scattering and some extra spots originating from these nanoparticles. These effects were not observed at all orientations due to the distinct OR of the matrix with the particles and their small dimensions. As an example, [111] orientation of the matrix is shown in Fig. 6a. Along $[100]_{Fe}$ orientation the additional reflections were observed occasionally, as shown in Fig. 6b and c taken from two different grains: in the ED pattern, shown in Fig. 6b, only body centered cubic (BCC) Fe spots are observed, while in Fig. 6c one can distinguish weak additional spots (marked by an arrow). This is an indication to a non-uniform distribution of the nano-sized oxides. Moreover, While tilting slightly away from the exact $[100]_{Fe}$ orientation, more extra spots appear, see Fig. 6d. Corresponding BF and DF images as obtained from an extra spot, shown in Fig. 6e and f, respectively, reveal the nano-sized particles that produce the extra reflections on the ED pattern.

The most complex data was received at [110] orientation of the matrix. In Fig. 7a-c, it can be seen that $[110]_{Fe}$ orientation contains many extra reflections and some diffuse scattering and that the amount of extra spots varies between matrix grains of the same orientation. In fact, Fig. 7a is a superposition of patterns b and c. ED pattern, shown in Fig. 7a, contains 3 phases. The most intense spots belong to the BCC Fe (see indices). Weaker spots can be attributed to two patterns, as marked on Fig. 7a. The DF images taken from g corresponding to a weak spot from each pattern (Fig. 7e and f) prove them to emerge from the finely dispersed nano-oxides. BF image is shown in Fig. 7d for reference. It can be concluded that pattern shown in Fig. 7a is a superposition of several different orientations/structures. Furthermore, some additional spots, circled on Fig. 7b, appear due to multiple scattering (they disappear while tilting around the corresponding reflection rows). All this makes an indexing in this case extremely difficult.

Fe ED patterns. Similar to those presented here. Were discussed in the literature as superimposed ED patters of Fe and its native oxides. To eliminate the doubt that the origin of the observed particles is surface oxidation of the TEM sample, we checked the density of the nano-sized particles, at the same Fe orientations and same grains, before and after cleaning the surface using the PIPS, and found them to be identical. Kuroda *et al.* [34], have studied the OR between the Fe substrate and a passive oxide film and reported their characteristics. The ED patterns, observed in the current study, were essentially identical to those reported in [34], allowing us to adopt their interpretation of the ED patterns. Kuroda *et al.* [34] indexed their ED patterns in terms of Fe_3O_4/Fe_2O_3 oxides, both with $MgAl_2O_4$-type spinel structure. The authors claim that it is difficult to distinguish between the two phases due to their similar structure and their close lattice parameters. They proposed Bain OR for the $[100]_{Fe}$ orientation, `*e.g.* $[100]_{Fe}//[100]_{oxide}$ and $(01\bar{1})_{Fe}//(010)_{oxide}$. Fig. 8a shows a simulation of the matrix and Fe_3O_4 with Bain OR. As can be seen, the simulation fits well the experimental pattern shown in Fig. 6c. At $[\bar{1}10]_{Fe}$, Kuroda *et al.* [33] proposed Kurdjumov-Sachs (K−S) OR [35], *e.g.* $[\bar{1}10]_{Fe}//[\bar{1}\bar{1}1]_{oxide}$ and $(111)_{Fe}//(101)_{oxide}$. Fig. 8b presents a simulation of the matrix and Fe_3O_4 with K−S OR. The simulation is very similar to pattern #1, shown in Fig. 7b (when multiple scattering is taken into account). It should be noted that in the work of Kuroda *et al.* [34], no extra reflections were observed at the $[111]_{Fe}$ orientation, which is in line with our observations. Moreover, they had also presented ED pattern with a slight misorientation from the exact $[100]_{Fe}$ zone axis, which was identical to the pattern

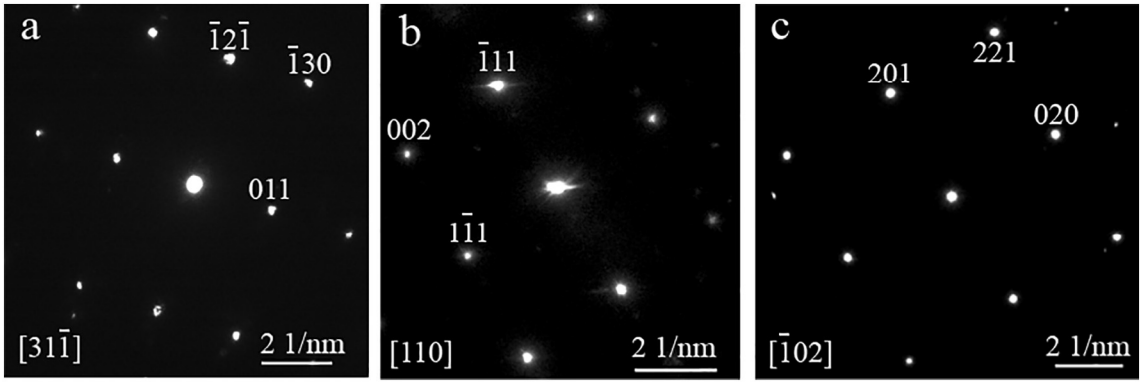

Fig. 5. ED patterns obtained from different large oxide particles in the bulk sample. These patterns were indexed as of a) [31$\bar{1}$], b) [110] and c) [$\bar{1}$02] zone axis patterns of the $YTiO_3$ structure. Some additional spots, originated by the Fe matrix, are visible on these ED patterns.

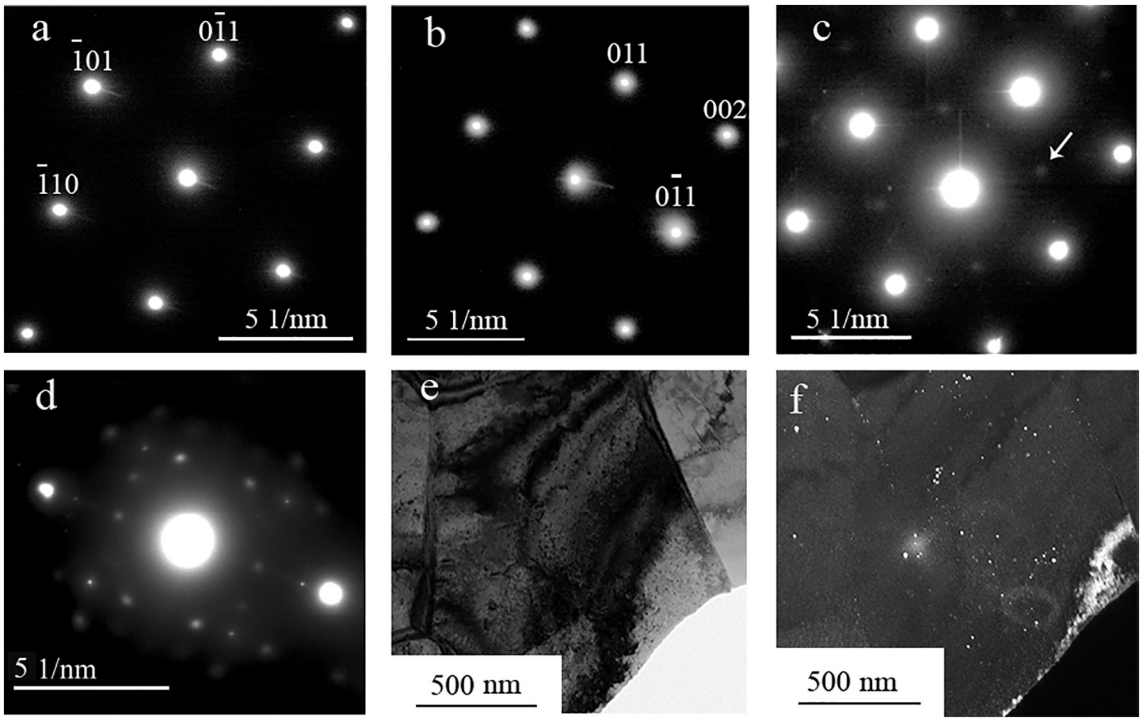

Fig. 6. a) $[111]_{Fe}$ ED pattern taken from a matrix grain shows no extra spots. (b) and (c) $[100]_{Fe}$ ED patterns taken from two Fe grains, yet only one displays extra spots ((c)-arrowed), illustrating the non-uniformity of the nano-oxide distribution. d) ED pattern slightly tilted away from the exact $[100]_{Fe}$ orientation, exhibits more extra-spots. e) BF and f) DF images taken at g, corresponding to extra spots, proving that they emerge from the nanoparticles.

shown in Fig. 6d. Thus, it is reasonable to conclude that the nano-sized oxides in the current study possess the $MgAl_2O_4$-type spinel structure with Bain and K–S ORs with the BCC Fe matrix, as reported in [34].

However, existence of nano-oxides with spinel structure does not provide an answer to all extra spots appearing at Fig. 7a. In fact, that particular pattern was taken at the thicker area of the TEM samples, thus some of the spots that appear in Fig. 7b (marked by a circle) do not belong to patterns #1 and #2 and result from dynamical (multiple) scattering [36,37]. Pattern #2, marked in Fig. 7a and shown in Fig. 7c, can be indexed in terms of the $YTiO_3$ with a distorted perovskite structure, referred earlier in this paper. Fig. 8c shows a simulation of the [110] orientation of the BCC Fe and [210] orientation of the $YTiO_3$ structure. This OR is $[110]_{Fe}//[210]_{oxide}$ and $(110)_{Fe}//(002)_{oxide}$. To the best of our knowledge, OR of this structure with the Fe (BCC) matrix was not reported earlier. However, this particular indexing is uncertain since pattern #2 could also be indexed in terms of spinel structure at the [$\bar{2}$11] orientation.

4. Discussion

The nanometric size of the oxides embedded in the Fe-rich matrix of the ODS steels and the fact that these particles tend to be non-stoichiometric makes their structure characterization challenging. The practice used by many researchers to conclude structure of the strengthening oxides from single orientation of ED or FFT of the HRTEM image may lead to erroneous conclusions. Here, thorough analysis allowed concluding that the studied 14%Cr ODS steel contains three types of dispersoids: very large TiC particles with a size of 100–200 nm, 50–150 nm $YTiO_3$ and Fe, Cr, Ti and Y spinel oxides, with a size of several to 20 nm. Table 3 summarizes the sizes and crystallographic data of the particles found in the studied steel.

The full characterization of the large (50–150 nm) oxides was challenging due to the contribution of Fe matrix to the ED patterns and EDS spectra. Furthermore, some ED patterns obtained from our samples could not be indexed in terms of reported Y-Ti-O phases, while others could be indexed in terms of more than one phase. To overcome these

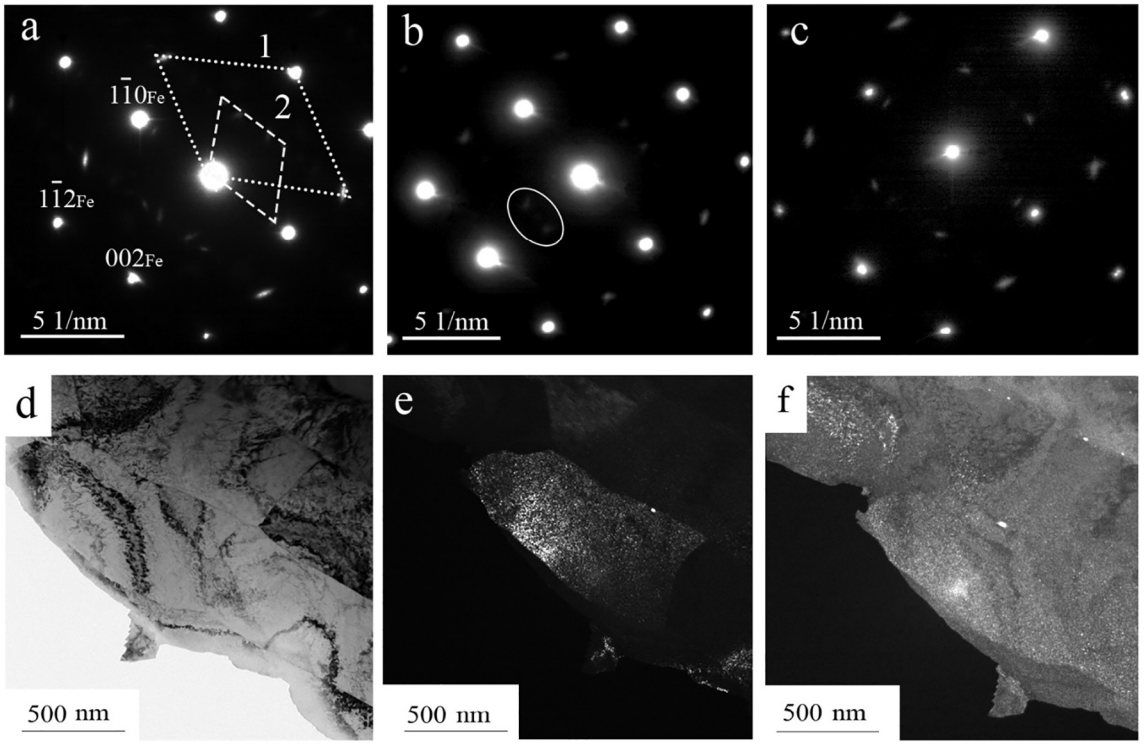

Fig. 7. a-c) ED patterns taken at $[110]_{Fe}$ orientation. Some extra spots originate from multiple scattering. Other extra reflections belong to the patterns marked as 1 and 2 on (a). While (b) and (c) show patterns 1 and 2 independently. d) BF image of the grain from which the ED pattern shown in (a), was taken. e) and f) are DF obtained at *g* belonging to patterns #1 and #2, respectively.

obstacles the particles in concern were isolated using extraction replica. EDT method allowed to conclude the structure of the large particles as $YTiO_3$ distorted perovskite. The lattice parameters, determined from the EDT data, allowed successful indexing of all ED patterns taken from the Y-Ti-O particles.

The nano-sized (3–20 nm) particles were most difficult to characterize. High resemblance of the complex ED patterns in our work to those reported by Kuroda *et al.* [34] led us to interpret the structure of the nano-oxides as $MgAl_2O_4$-type spinel with K—S and Bain OR with the Fe matrix. This interpretation was verified by the good fit between simulated and measured ED patterns. We found only one article [39] reporting the existence of spinel structure in the ODS steels, where the

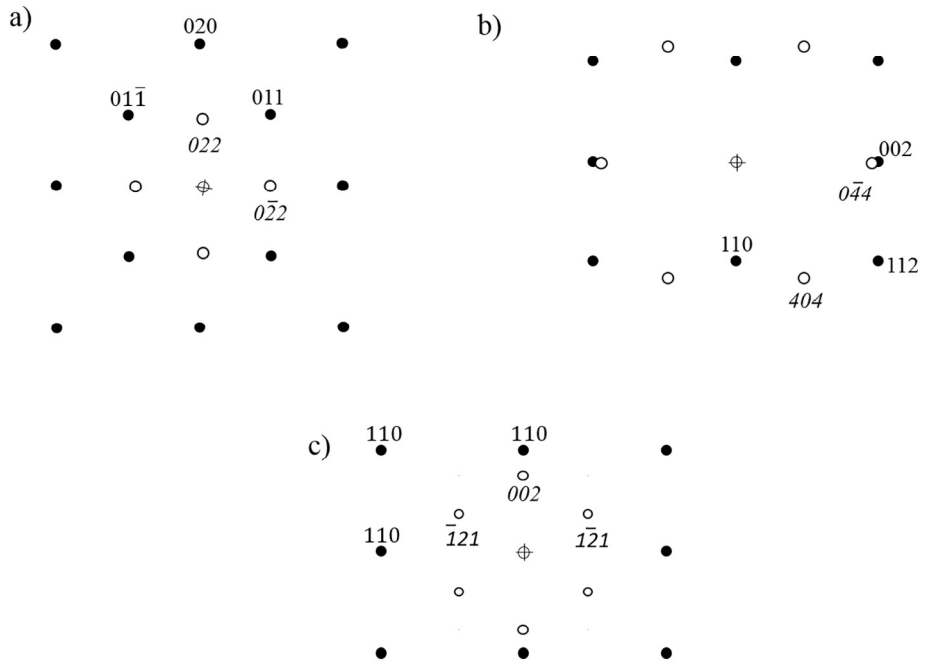

Fig. 8. Superimposed ED patterns, prepared using CaRIne Crystallography software [38], simulating: a) $[100]_{Fe}$ and $[100]_{spinel\ oxide}$ according to the Bain type relationship and b) $[\bar{1}10]_{Fe}$ and $[\bar{1}11]_{spinel\ oxide}$ according to the Kurdjumov-Sachs type relationship. c) $[110]_{Fe}$ and $[210]_{YTiO_3}$. Black full dots and empty circles correspond to Fe and oxide's reflections, respectively. Matrix reflections are indicated by regular font, while oxide's indices are italized.

Table 3
Structural characteristics of particles found to be present in the studied ODS steel.

Type of particle	Structure	Lattice parameters [Å]	Size distribution [nm]
TiC	TiC structure type, $Fm\bar{3}m$	a = 4.33 [27]	100–200
$YTiO_3$	$GdFeO_3$ (distorted perovskite) structure type, $Pnmn$	a = 5.46, b = 7.66, c = 5.28 [current work]	50–150
Non-stoichiometric Fe (Cr,Ti,Y)O	$MgAl_2O_4$ (spinel) structure type, $Fd\bar{3}m$	a = 8.4 [34]	3–20

particles, 30–50 nm in size, were identified as $TiCr_2O_4$. In general, spinel structure is described as AB_2O_4, and in the case of Fe_3O_4 (magnetite), the chemical composition is $Fe^{2+}Fe_2{}^{3+}O_4$. The solubility of Ti in magnetite is relatively high [40] and Ti-rich magnetite can change its stoichiometry to Fe_2TiO_4 (also called Ulvöspinel). Cr also has a high solubility in magnetite [41] and can change its stoichiometry to Fe_2CrO_4. In both cases, the structure remains the same as the Fe_3O_4 and the lattice parameter slightly changes from $a_{Fe_3O_4}=8.390$ Å [42] to $a_{Fe_2TiO_4}=8.535$ Å [43] in the case of Ti addition, or in the case of Cr addition: $a_{Fe_2CrO_4}=8.379$ Å [41]. Such differences in lattice parameters are undetectable by ED due to the diffuse nature of the spots. APT results show that in the current steel the nano oxides were composed of Fe, Ti, Cr, O and a small amount of Y. Thus, it can be assumed that the nano-oxides that exist in the studied 14%Cr ODS steel are non-stoichiometric Fe(Cr,Ti,Y)O with an $MgAl_2O_4$-type spinel structure. Since out of three distinctive groups of particles, detected in the current work, the nano-oxides were the most densely distributed, and have distinct OR with the matrix, we believe that this population of oxides has a major effect on the mechanical properties of this steel.

In general, the type of oxide particles existing in ODS steels vary from one steel to another. Even ODS steels with very similar composition may exhibit differences in their oxides population. For example, Bhattacharyya *et al.* [5] found three types of oxide particles in the 14Cr-3W-0.4Ti-0.25Y_2O_3 ODS steel: large $CrTiO_3$, small non-stoichiometric Y, Ti, O with a structure somewhat similar to the Y_2TiO_5 and smaller particles, which did not fit any known Y-Ti-oxide structures. Unifantowicz *et al.* [18] studied similar composition and found large Cr-Ti-O, Cr—N particles and smaller ones with the distorted $YTiO_3$ perovskite structure. Also, in a similar composition, Hirata *et al.* [19] found non-stoichiometric Ti(Y,Fe,Cr)O with a defective NaCl structure and London *et al.* [44] found $Y_2Ti_2O_7$ particles surrounded by a Cr-rich shell. These reports along with the results of the current study indicate that not only the composition of the steel governs the types of oxides formed in the steel, but other parameters, probably related to the fabrication process. Among such parameters, which are not easy to fully control, are the process environment and the extent of surface oxidation of the precursor metallic powder particles. This surface oxide layer may undergo processes similar to those reported for Yttria particles, namely, amorphization and mechanical dissolution in the metallic matrix [45] and subsequent crystallization during hot consolidation. Such mechanism may also explain the distinctive OR observed in the current study, which implies that the Fe(Cr,Ti,Y)O particles were formed by a precipitation mechanism.

5. Conclusions

The particles existing in the studied ODS steel were classified into three populations. The largest and less frequent particles (100–200 nm) were determined as TiC. Another population of large particles (50–150 nm) was studied using the EDT method and characterized unambiguously as $YTiO_3$ with a distorted perovskite structure. Lattice parameters of these oxides were refined. Orientation relationship of the $YTiO_3$ structure and Fe matrix was determined as $[110]_{Fe}//[210]_{oxide}$ and $(110)_{Fe}//(002)_{oxide}$. The smallest (3–20 nm) and most frequent particles, were identified by APT and superimposed matrix/oxide ED patterns as Fe(Cr,Ti,Y)O with an $MgAl_2O_4$-type spinel structure. These particles possessed Bain OR with the matrix along the $[100]_{Fe}$ direction, and K—S OR along the $[\bar{1}10]_{Fe}$ direction. The high density of the nano-oxides and their OR with the matrix imply that they may have a major contribution to the strengthening of the studied 14%Cr ODS steel.

Acknowledgments

We thank Dr. Dennis Sornin and the CEA/DEN/DANS for providing the ODS alloy. LM and MP thank the JRC funding of the project. Atom probe tomography study was supported by the Russian Science Foundation under grant 17-19-01696 and performed at the NRC "Kurchatov Institute"– ITEP.

Data availability

The raw/processed data required to reproduce these findings cannot be shared at this time as the data also forms part of an ongoing study.

References

[1] A. Kohyama, M. Seki, K. Abe, T. Muroga, H. Matsui, S. Jitsukawa, S. Matsuda, Interactions between fusion materials R&D and other technologies, J. Nucl. Mater. 283–287 (2000) 20–27, https://doi.org/10.1016/S0022-3115(00)00156-2.
[2] G.R. Odette, M.J. Alinger, B.D. Wirth, Recent developments in irradiation-resistant steels, Annu. Rev. Mater. Res. 38 (2008) 471–503, https://doi.org/10.1146/annurev.matsci.38.060407.130315.
[3] S. Ukai, M. Fujiwara, Perspective of ODS alloys application in nuclear environments, J. Nucl. Mater. 307–311 (2002) 749–757, https://doi.org/10.1016/S0022-3115(02)01043-7.
[4] S. Chen, K. Tadaki, Y. Wang, N. Hashimoto, S. Ohnuki, Effect of oxide particles and pre-implanted helium on defect evolution during electron irradiation, Mater. Trans. 55 (2014) 443–446, https://doi.org/10.2320/matertrans.MD201318.
[5] D. Bhattacharyya, P. Dickerson, S.A. Maloy, A. Misra, M.A. Nastasi, G.R. Odette, On the structure and chemistry of complex oxide nanofeatures in nanostructured ferritic alloy U14YWT, Philos. Mag. 92 (2012) 2089–2107.
[6] M.K. Miller, D.T. Hoelzer, E.A. Kenik, K.F. Russell, Stability of ferritic MA/ODS alloys at high temperatures, Intermetallics 13 (2005) 387–392, https://doi.org/10.1016/j.intermet.2004.07.036.
[7] T. Okuda, M. Fujiwara, Dispersion behaviour of oxide particles in mechanically alloyed ODS steel, J. Mater. Sci. Lett. 14 (1995) 1600–1603.
[8] T. Liu, H. Shen, C. Wang, W. Chou, Structure evolution of Y_2O_3 nanoparticle/Fe composite during mechanical milling and annealing, Mater. Int. 23 (2013) 434–439, https://doi.org/10.1016/j.pnsc.2013.06.009.
[9] K. Oka, S. Ohnuki, S. Yamashita, N. Akasaka, S. Ohtsuka, H. Tanigawa, Structure of nano-size oxides in ODS steels and its stability under electron irradiation, Mater. Trans. 48 (2007) 2563–2566.
[10] N. Akasaka, S. Yamashita, T. Yoshitake, S. Ukai, A. Kimura, Microstructural changes of neutron irradiated ODS ferritic and martensitic steels, J. Nucl. Mater. 329–333 ((2004) 1053–1056.
[11] V.L. Arbuzov, B.N. Goshchitskii, V.V. Sagaradze, S.E. Danilov, A.E. Kar'kin, Accumulation and annealing of radiation defects under low-temperature electron and neutron irradiation of ODS steel and Fe-Cr alloys, Phys. Met. Metallogr. 110 (2010) 366–377.
[12] H. Sakasegawa, L. Chaffron, F. Legendre, L. Boulanger, T. Cozzika, M. Brocq, Y. de Carlan, Correlation between chemical composition and size of very small oxide particles in the MA957 ODS ferritic alloy, J. Nucl. Mater. 384 (2009) 115–118, https://doi.org/10.1016/j.jnucmat.2008.11.001.
[13] J. Ribis, Y. de Carlan, Interfacial strained structure and orientation relationships of the nanosized oxide particles deduced from elasticity-driven morphology in oxide dispersion strengthened materials, Acta Mater. 60 (2012) 238–252.
[14] M. Klimiankou, R. Lindau, A. Moslang, TEM characterization of structure and composition of nanosized ODS particles in reduced activation ferritic-martensitic steels, J. Nucl. Mater. 329–333 (2004) 347–351.
[15] P. Jegadeesan, S. Amirthapandian, G. Kaur, S. Chandra, B.K. Panigrahi, Characterization of M-O bonds in Y2Ti2O7 and Y2TiO5 with EELS, Phys. Status Solidi Basic Res. 252 (2015) 206–211, https://doi.org/10.1002/pssb.201451297.
[16] H. Sakasegawa, F. Legendre, L. Boulanger, M. Brocq, L. Chaffron, T. Cozzika, J. Malaplate, J. Henry, Y. de Carlan, Stability of non-stoichiometric clusters in the MA957 ODS ferrtic alloy, J. Nucl. Mater. 417 (2011) 229–232, https://doi.org/10.1016/j.jnucmat.2010.12.056.
[17] Y. Wu, E. Haney, N. Cunningham, R.G. Odette, Transmission electron microscopy characterization of the structure and composition of the nanofeatures in

nanostructured ferritic alloy MA957, Acta Mater. 60 (2012) 3456–3468.
[18] P. Unifantowicz, T. Płociński, C.A. Williams, R. Schäublin, N. Baluc, Structure of complex oxide nanoparticles in a Fe–14Cr–2W–0.3Ti–0.3Y_2O_3 ODS RAF steel, J. Nucl. Mater. 442 (2013) S158–S163, https://doi.org/10.1016/j.jnucmat.2013.04.048.
[19] A. Hirata, T. Fujita, Y.R. Wen, J.H. Schneibel, C.T. Liu, M.W. Chen, Atomic structure of nanoclusters in oxide-dispersion-strengthened steels, Nat. Mater. 10 (2011) 922–926.
[20] A. Rouffie, Comprehension et mod´elisation de la rupture fragile des aciers renforc´es par nano-pr'ecipitation: effets de texture, de vieillissement et de composition, (2014).
[21] J. Boutard, V. Badjeck, L. Barguet, C. Barouh, A. Bhattacharya, Y. Colignon, C. Hatzoglou, M. Loyer-Prost, A.L. Rouffié, N. Sallez, H. Salmon-Legagneur, T. Schuler, Oxide dispersion strengthened ferritic steels: a basic research joint program in France, J. Nucl. Mater. 455 (2014) 605–611, https://doi.org/10.1016/j.jnucmat.2014.08.059.
[22] M. Gemmi, P. Oleynikov, Scanning reciprocal space for solving unknown structures: energy filtered diffraction tomography and rotation diffraction tomography methods, Zeitschrift Fur Krist 228 (2013) 51–58, https://doi.org/10.1524/zkri.2013.1559.
[23] S.V. Rogozhkin, A.A. Aleev, A.A. Lukyanchuk, A.S. Shutov, O.A. Raznitsyn, S.E. Kirillov, An atom probe tomography prototype with laser evaporation, Instruments Exp. Tech. 60 (2017) 428–433, https://doi.org/10.1134/S002044121702021X.
[24] M.K. Miller, Atom Probe Tomography: Analysis at the Atomic Level, Kluwer Acad, New York, 2000, https://doi.org/10.1093/brain/114.4.2019.
[25] A. Cerezo, L. Davin, Aspects of the observation of clusters in the 3-dimensional atom probe, Surf. Interface Anal. 39 (2007) 184–188, https://doi.org/10.1002/sia.
[26] J.M. Hyde, E.A. Marquis, K.B. Wilford, T.J. Williams, A sensitivity analysis of the maximum separation method for the characterisation of solute clusters, Ultramicroscopy 111 (2011) 440–447, https://doi.org/10.1016/j.ultramic.2010.12.015.
[27] A.N. Christensen, A neutron diffraction investigation on single crystals of titanium oxide, zirconium carbide and hafnium nitride, Acta Chem. Scand. A 29 (1975) 563, https://doi.org/10.3891/acta.chem.scand.29a-0563.
[28] Y. Wu, J. Ciston, S. Kraemer, N. Bailey, G.R. Odette, P. Hosemann, The crystal structure, orientation relationships and interfaces of the nanoscale oxides in nanostructured ferritic alloys, Acta Mater. 111 (2016) 108–115, https://doi.org/10.1016/j.actamat.2016.03.031.
[29] A.S. Eggeman, R. Krakow, P.A. Midgley, Scanning precession electron tomography for three-dimensional nanoscale orientation imaging and crystallographic analysis, Nat. Commun. 6 (2015) 1–7, https://doi.org/10.1038/ncomms8267.
[30] L. Meshi, S. Samuha, Characterization of atomic structures of nanosized intermetallic compounds using electron diffraction methods, Adv. Mater. 30 (2018) 1–7, https://doi.org/10.1002/adma.201706704.
[31] U. Kolb, T. Gorelik, C. Kübel, M.T. Otten, D. Hubert, Towards automated diffraction tomography: part I-data acquisition, Ultramicroscopy 107 (2007) 507–513, https://doi.org/10.1016/j.ultramic.2006.10.007.
[32] U. Kolb, T. Gorelik, M.T. Otten, Towards automated diffraction tomography. Part II — cell parameter determination, Ultramicroscopy 108 (2008) 763–772, https://doi.org/10.1016/j.ultramic.2007.12.002.
[33] "PDF4+" Commercial Database of the International Center for Diffraction Data, ICDD, 2016.
[34] K. Kuroda, B.D. Cahan, T.E. Mitchell, Electron diffraction study of the passive film on Iron, J. Electrochem. Soc. 129 (1982) 2163, https://doi.org/10.1149/1.2119671.
[35] G. Kurdjumov, G. Sachs, Zeitschrift Für Phys. 64 (1930) 325.
[36] O. Moshka, M. Pinkas, E. Brosh, V. Ezersky, L. Meshi, Addressing the issue of precipitates in maraging steels - unambiguous answer, Mater. Sci. Eng. A 638 (2015) 232–239, https://doi.org/10.1016/j.msea.2015.04.067.
[37] J.W. Edington, Practical electron microscopy in metarials science, in: Pract. Electron Microsc. Metarials Sci., 1976: p. 89.
[38] C. Boudias, D. Monceau, CaRIne Crystallography 3.1, DIVERGENT S.a., Cent. Transf. 60200 Compiègne, Fr, (1989).
[39] C. Lu, Z. Lu, R. Xie, C. Liu, L. Wang, Microstructure of a 14Cr-ODS ferritic steel before and after helium ion implantation, J. Nucl. Mater. 455 (2014) 366–370, https://doi.org/10.1016/j.jnucmat.2014.06.065.
[40] A.F. Buddington, D.H. Lindsley, Iron-titanium oxide minerals and synthetic equivalents, J. Petrol. 5 (1964) 310–357.
[41] J. Ma, V.O. Garlea, A. Rondinone, A.A. Aczel, S. Calder, C. Cruz, R. Sinclair, W. Tian, S. Chi, A. Kiswandhi, J.S. Brooks, H.D. Zhou, M. Matsuda, Magnetic and structural phase transitions in the spinel compound Fe 1 + XCr2-xO4, Phys. Rev. B - Condens. Matter Mater. Phys. 89 (2014) 1–9.
[42] F. De Boer, J.H. Van Santen, E.J.W. Verwey, The electrostatic contribution to the lattice energy of some ordered spinels, J. Chem. Phys. 18 (1950) 1032–1034, https://doi.org/10.1063/1.1747852.
[43] A. Masanori, N. Shoichiro, Contribution of Mo^{4+} ions to the magnetic interaction in Fe2MoxTi1-xO4, J. Phys. Soc. Jpn. 38 (1975) 1779.
[44] A.J. London, S. Santra, S. Amirthapandian, B.K. Panigrahi, R.M. Sarguna, S. Balaji, R. Vijay, C.S. Sundar, S. Lozano-Perez, C.R.M. Grovenor, Effect of Ti and Cr on dispersion, structure and composition of oxide nano-particles in model ODS alloys, Acta Mater. 97 (2015) 223–233.
[45] L.L. Hsiung, M.J. Fluss, S.J. Tumey, B.W. Choi, Y. Serruys, F. Willaime, A. Kimura, Formation mechanism and the role of nanoparticles in Fe-Cr ODS steels developed for radiation tolerance, Phys. Rev. B - Condens. Matter Mater. Phys. 82 (2010) 1–13, https://doi.org/10.1103/PhysRevB.82.184103.